

Performance Evaluation of a Position-Sensitive SiPM-based Gamma Camera for Intraoperative Imaging

Aramis Raiola^{1*}, Fabio Acerbi², Cyril Alispach¹,
Domenico della Volpe¹, Hossein Arabi³, Alberto Gola²,
Habib Zaidi^{3,4,5,6}

^{1*}Département de Physique Nucléaire et Corpusculaire (DPNC),
Université de Genève, quai Ernest-Ansermet 24, Geneva, 1211,
Switzerland.

²Center for Sensor and Devices (SD), Fondazione Bruno Kessler
(FBK), Via Sommarive 18, Trento, 38122, Italy.

³Division of Nuclear Medicine and Molecular Imaging, Geneva
University Hospital (HUG), Geneva, 1211, Switzerland.

⁴Department of Nuclear Medicine and Molecular Imaging, University of
Groningen, University Medical Center Groningen, 9700 RB, Groningen,
Netherlands.

⁵Department of Nuclear Medicine, University of Southern Denmark,
DK-500, Odense, Denmark.

⁶University Research and Innovation Center, Óbuda University,
Budapest, Hungary.

*Corresponding author(s). E-mail(s): aramis.raiola@unige.ch;

Contributing authors: acerbi@fbk.eu; cyril.alispach@unige.ch;
domenico.dellavolpe@unige.ch; hossein.arabi@unige.ch; gola@fbk.eu;
habib.zaidi@hug.ch;

Abstract

Context: The POSiCS camera is a handheld, small field-of-view gamma camera developed for multipurpose use in radio-guided surgery (RGS), with sentinel lymph node biopsy (SLNB) as its benchmark application. This compact and lightweight detector (weighing approximately **350 g**) can map tissues labeled

with ^{99m}Tc nanocolloids and guide surgeons to the location of target lesions. By enabling intraoperative visualization in close proximity to the surgical field, its primary objective is to minimize surgical interventional invasiveness and operative time, thereby enhancing localization accuracy and reducing the incidence of post-operative complications. The design and components of the POSiCS camera emphasize ergonomic handling and compactness, providing, at the same time, rapid image formation and a spatial resolution of a few millimeters. These features are compatible with routine operating-room workflow, including wireless communication with the computer and a real-time display to support surgeon decision-making.

Methods: The camera was developed and assessed in two interchangeable hardware configurations: high-sensitivity and high-resolution, to provide flexibility according to application-specific requirements. Performance characterization employed Flood phantom (flat) sources of ^{99m}Tc and point sources of ^{57}Co . The response to ^{177}Lu was also investigated, given its increasing role in theranostics. Tests on the device were aimed at assessing the main performance parameters, such as extrinsic spatial resolution, energy resolution, and sensitivity. Moreover, the camera shielding was also evaluated, as well as the device's response to gamma rays of different energy.

Results: The spatial resolution measured at a source–detector distance of **0 cm** was $1.9 \pm 0.1 \text{ mm}$ for the high sensitivity mode and $1.4 \pm 0.1 \text{ mm}$ for the high resolution mode. The system sensitivity at **2 cm** was evaluated as $481 \pm 14 \text{ cps/MBq}$ (high sensitivity) and $134 \pm 8 \text{ cps/MBq}$ (high resolution). For both working modes, we report an energy resolution of approximately 20%, even though the high-resolution collimator exhibits an increased scattered component due to the larger amount of tungsten.

Keywords: Intraoperative Gamma Camera, Nuclear Medicine, Radio Guided Surgery, Sentinel Lymph Nodes Biopsy, Radio Occult Lesion Localization, Silicon Photomultipliers

1 Introduction

Radio-guided surgery (RGS), including intraoperative techniques such as sentinel lymph node biopsy (SLNB) and radioguided occult lesion localization (ROLL), is a widely adopted approach, particularly in the surgical management of breast cancer and cutaneous melanoma. [1, 2]. Despite the availability of well-established alternatives to RGS (such as Fluorescence-Guided Surgery (FGS) or Ultrasound-Guided Surgery), the preoperative administration of radio-labeled nanocolloids remains one of the most widely used techniques for intraoperative localization of oncological lesions. This is due to the extensive range of gamma rays in living tissues, which allows for the direct detection and localization of activity hot-spots from outside the patient's body [1, 2, 3].

The state-of-the-art practice in SLNB and ROLL is based on 1D probes to localize lesions or sentinel lymph nodes (SLNs) [4]. Although this approach has been proven reliable by clinically comparing preoperative lymphoscintigraphies with the number of SLNs localized through a probe-based search, probes still have some disadvantages.

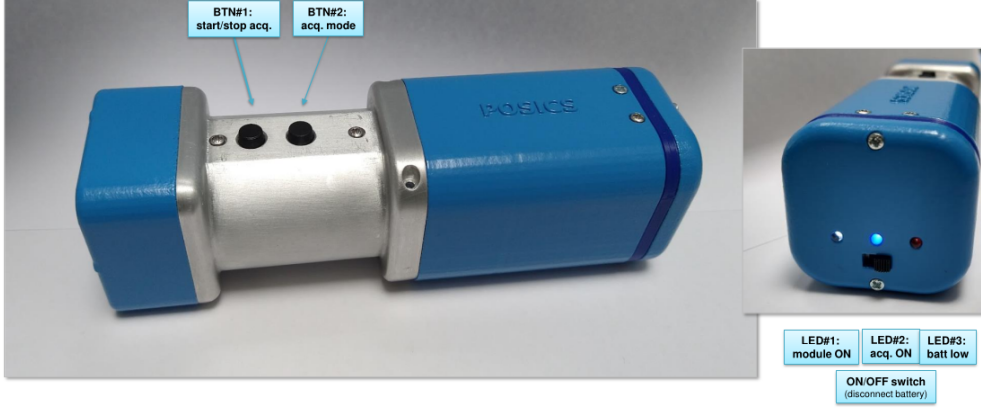


Fig. 1 Prototype wireless module of the POSiCS gamma camera.

For this reason, an increasing number of 2D Intraoperative Gamma Cameras (IGCs), also known as Small Field of View (SFOV) gamma cameras, have been developed in the last decades [5, 6]. This trend has been thoroughly studied in recent years, thanks to the comprehensive reviews in the field of IGCs, such as [7] and a more recent follow-up [4]. The main advantages of cameras are their imaging capabilities, which allow surgeons to localize hot spots near the “blast zone” (radiotracer injection site) and provide a method to verify post-excision images to ensure that the target lymph node or lesion was entirely resected [8, 9]. Additionally, imaging is intuitive and does not require the specific and lengthy training needed to become proficient with 1D probes. It has also been shown that 2D imaging of oncological lesions can reduce surgery duration, as it facilitates the localization of target tissues more quickly [8, 10].

The device is equipped with two interchangeable collimators: a short low-energy high-sensitivity (LEHS) collimator and a longer low-energy high-resolution (LEHR) collimator, enabling dual operating modes that can be selected intraoperatively to adapt to different clinical needs during surgery. Optimized for detecting photons at 140.5 keV, corresponding to the emission energy of $^{99\text{m}}\text{Tc}$ [11], the standard radionuclide used in RGS, the POSiCS camera exhibits enhanced performance relative to existing systems. This improvement is due in part to a novel position-sensitive silicon photomultiplier (SiPM) technology developed by Fondazione Bruno Kessler (FBK). The device performs center-of-gravity (CoG) light-position reconstruction, achieving a nominal spatial resolution of about $100\text{ }\mu\text{m}$ [12, 13]. Thanks to a “smart-channel” configuration, the SiPM array requires only 8 readout channels over a $30.8 \times 30.8\text{ mm}^2$ area for a 3×3 LG-SiPMs array [12]. This architecture reduces data throughput, provides fast timing, and enables wireless communication with the processing unit, thereby eliminating cumbersome cables during surgery. Moreover, the use of LG-SiPMs facilitates a battery-powered module, owing to the low power consumption of solid-state photodetectors [12, 14, 15].

In this article, we present the results of the first performance studies on the prototype POSiCS module. In Section 2, we describe the main components of the camera

and its advantages in the field of RGS. In Section 3, we present the experimental methods adopted to measure the main performance parameters of the camera with both collimators. The tests were inspired by the 2023 NEMA standards for gamma camera qualification [16]. However, as these standards are primarily designed for large clinical scanners, only a subset of the proposed measurements and procedures applies to our device, given its specific design and use case. In Section 4, the results of the tests are displayed and commented. Conclusively, in Section 4.6, we provide an overall discussion of the obtained results, while in Section 5, we offer a brief outlook and prospects.

2 The POSiCS camera

2.1 General operation

The POSiCS camera is a handheld gamma-ray imaging detector, based on a LYSO:Ce scintillator and a 3×3 array of position-sensitive SiPMs (LG-SiPMs).

For each detected event, the 8 signals from the SiPMs are digitized by an onboard ADC and processed by a microcontroller, which calculates the (x, y) position of the gamma-ray interaction. The position (x,y coordinates), the energy of the event (sum of the channels' charge output), and the time stamp information are transmitted wirelessly to a PC, where image correction and quality enhancement algorithms are applied to produce the final image.

The current camera module has a total length of 147 mm (155 mm with the LEHR collimator mounted), with a Field of View (FOV) of $30.8 \times 30.8 \text{ mm}^2$. From this, we define a Useful Field of View (UFOV) of $28.6 \times 28.6 \text{ mm}^2$. The module total weight is 313 g (with the LEHS collimator) and 381 g (with the LEHR collimator). Further technical details about the camera are found in the POSiCS camera's technical paper [17].

2.2 Collimator geometry

The POSiCS camera is equipped with two interchangeable parallel-hole collimators: one targeting high spatial resolution (LEHR) for surgical procedures that require precise identification of target lesion margins, and the other designed to achieve high sensitivity (LEHS) for faster imaging times, even at low injected activities. The different parameters that qualify both objects were chosen through theoretical calculations and simulations using GATE [18]. Due to its high atomic number (implying a short attenuation length) and good resistance to shocks [4], tungsten was chosen as a material. All the collimator parameters were chosen to ensure a septal penetration probability of less than 5% [19, 20]. The collimator was designed with external shielding walls that extend beyond the collimator holes and support the scintillator, reducing the amount of gamma rays entering from the side of the camera.

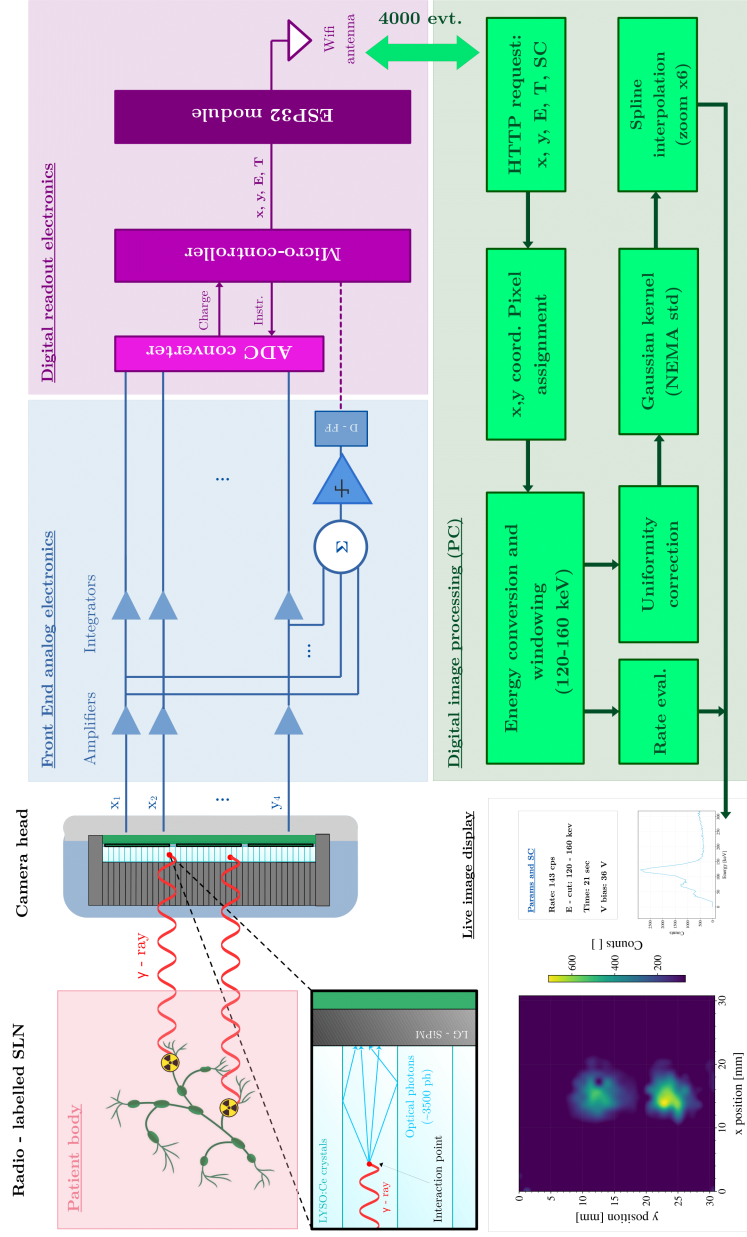


Fig. 2 Scheme of the full operation and calibration pipeline of the POSiCS camera, from the gamma-ray emission by radio-labelled tissues, to the final image treatment and enhancement, with the possibility of live displaying the reconstructed image.

2.3 LYSO scintillator approach

The radiation-sensitive component of the POSiCS camera is a pixelated LYSO:Ce scintillator. This Lutetium-based crystal is typically used in Positron Emission Tomography (PET) scanners due to its fast decay time (~ 40 ns), large light yield (≥ 32000 ph MeV $^{-1}$), and high density [21]. The camera was therefore built using a very thin crystal (a few millimeters thick), keeping a high photoelectric absorption probability at 140.5 keV. The scintillator is pixelated in a 30×30 matrix. Each pixel is coated with a BaSO₄ reflector to increase light collection on the light detector.

A peculiarity of LYSO:Ce is its intrinsic radioactivity due to the natural 2.6% abundance of ^{176}Lu isotope, which decays into ^{176}Hf through a β^- decay. The process is followed by the emission of three gamma rays at energies: 88 keV, 202 keV, and 307 keV, which can interact within the crystal itself [22, 23]. The presence of this isotope establishes a background activity within the camera FOV at about 420 cps, which is mainly eliminated through energy window selection and subtracted during image correction. This feature is often cited as being suited for self-calibration in PET scanners and can represent an advantage in this direction in the future [24]. The LYSO:Ce intrinsic spectrum reconstructed with the POSiCS camera is displayed in Figure 3.

2.4 LG-SiPMs photodetector

Until 2013, reviews in the field of IGCs showed a trend toward implementing Position-Sensitive (PS-) PMTs in SFOV gamma cameras [7]. At the same time, most recent reviews highlight a shift in the past decade toward using SiPMs for the optical readout of scintillator crystals in IGCs [4]. This transition is driven by the advantages of solid-state detectors, including low power consumption, compactness, high quantum efficiency, and insensitivity to magnetic fields.

In the current context of light detectors for IGCs, POSiCS proposes an innovative approach by moving towards PS-SiPMs, leveraging the new Linearly Graded SiPMs technology (LG-SiPMs) designed and produced by FBK [25, 12, 26]. Through an array of 3×3 LG-SiPMs with peak sensitivity at 420 nm, an active area of about 10×10 mm² per sensor, and microcell pitch of 25 μm , it is possible to reconstruct the position of each scintillation event, through a weighted charge (and amplitude) distribution towards the output channels. Each Single Photon Avalanche Diode (SPAD) composing the SiPM is connected to a resistive network, which performs a light spot CoG reconstruction, encoded in the relative amount of charge output by each readout channel [17, 12]. This Anger CoG reconstruction is typically used between SiPMs or PMTs in standard gamma cameras, but this approach is implemented at the single microcell level within the POSiCS camera. The 3×3 array configuration, with the "smart channel" approach (see [12]), allows CoG reconstruction with only 8 readout channels: 4 encoding for the x coordinate (x_1, x_2, x_3, x_4) and 4 reconstructing the y coordinate (y_1, y_2, y_3, y_4). More precisely, position reconstruction is performed as follows:

$$x_{pos} = \frac{x_1 + \frac{1}{3}(x_3 - x_2) - x_4}{x_1 + x_2 + x_3 + x_4}, \quad (1a)$$

$$y_{pos} = \frac{y_1 + \frac{1}{3}(y_3 - y_2) - y_4}{y_1 + y_2 + y_3 + y_4}. \quad (1b)$$

This weighted position calculation is performed directly within the camera digital electronics, which in turn sends the reconstructed positions through a wireless connection. This photon detector demonstrated exceptional intrinsic precision, achieving a resolution of a few hundred microns [12, 13].

The limited number of channels enables a fast and straightforward readout, allowing for wireless data transmission to the computer before applying the necessary image quality processing.

2.5 Approach to image reconstruction

When a scintillation event occurs, the output charge from each of the eight channels is amplified by dedicated transimpedance amplifiers (TIAs). The summed signal is simultaneously processed by a comparator, which enables signal integration only if a user-defined threshold is exceeded. Once this condition is met, the charge of each channel is integrated and digitized by an eight-channel analog-to-digital converter (ADC). The microcontroller (μ C) then calculates the total event energy E (in ADC counts), records the event timestamp, and computes the x - and y -coordinates using Equation 1. In addition, the μ C provides slow-control (SC) data to the system, including the bias voltage status, absorbed current, module temperature, battery status, and other relevant operational parameters. A block diagram of the analog and digital electronics of the POSiCS wireless module is shown in Figure 2. Each event consists of four parameters: the x and y scintillation light center-of-gravity (CoG) coordinates, the energy E in analog-to-digital converter (ADC) counts, and the timestamp T , represented as (x, y, E, T) . The microcontroller (μ C) transmits these events to an external computer via an ESP32 module, in packets containing 4000 events. The user can retrieve these packets through HTTP GET requests, as well as access the slow-control (SC) information.¹

Reconstructed images are corrected using a three-step calibration and correction procedure. First, once the incident position of a gamma ray is determined (x, y CoG coordinates), the event is assigned to the corresponding camera pixel associated with the scintillator crystal encompassing the interaction position, whose physical dimensions are precisely known (linearity correction). This spatial mapping is established through a flood-field calibration scan, which serves as the primary calibration step before operating the camera.

Second, a pixel-by-pixel energy calibration is performed. In this step, a scaling coefficient is applied to convert the SiPMs charge response into a physical energy. Due to non-uniform light collection across certain regions of the FOV, as well as slight variations in the gain and response characteristics of the SiPMs forming the optical readout array, each pixel is assigned an individually determined conversion coefficient from ADC counts (digitized charge) to a physical energy in keV. Following

¹The camera settings are also transmitted through the same ESP32 module via HTTP POST requests, which configure the digital-to-analog converters (DACs). These commands include the bias voltage setting, comparator threshold level, and the integration delay and time width.

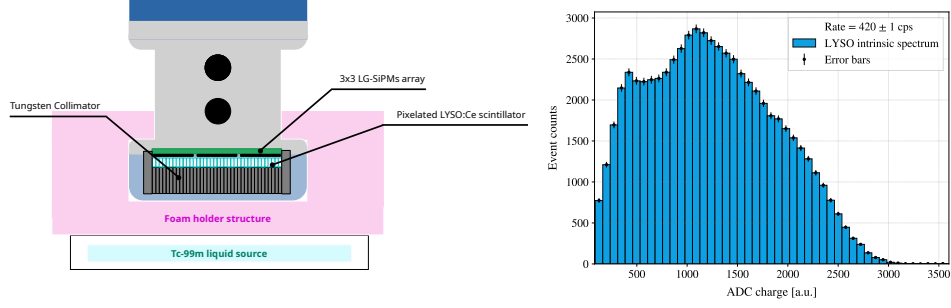


Fig. 3 Left: Scheme of the Flood map setup used in this work. The estimated distance from the collimator entrance to the center of the cavity is 2 cm. **Right:** LYSO:Ce scintillator intrinsic radioactivity spectrum registered with POSiCS. The structure of the spectrum depends on the crystal volume and shape, which in turn determines the probability of absorbing the emitted γ -rays (in coincidence). The long tails are due to the absorption of the initial β particle and are therefore shaped after the β -emission spectrum [23].

this step, a user-defined energy window can be applied in software to selectively retain events consistent with photoelectric interactions, thereby suppressing contributions from Compton-scattered events that occur either within the LYSO crystal or in the surrounding environment.

Finally, a uniformity correction is applied to the reconstructed image to compensate for spatial sensitivity variations. This step enhances the signal in regions typically exhibiting under-response, such as those corresponding to interstitial gaps between SiPMs or at the periphery of the camera field of view, thereby ensuring a more homogeneous image representation.

With this system, it is possible to live display images with a delay in the order of 1 or 2 seconds. Final images are usually enhanced with a Gaussian kernel, to smooth statistical variations in the image shape (especially useful in low-activity scenarios, where high statistics are difficult to achieve). The convolution kernel is defined as:

$$w_{k,l} = \frac{1}{16} \begin{bmatrix} 1 & 2 & 1 \\ 2 & 4 & 2 \\ 1 & 2 & 1 \end{bmatrix} \quad (2)$$

Following the 2023 guideline presented in the NEMA standards for the validation of gamma cameras [16]. To conclude, the smoothed image is treated with a spline interpolation of order 2, with a zooming factor of 6. A scheme of the full data reconstruction and image enhancement pipeline is presented in Figure 2.

3 Experimental methods

The POSiCS camera underwent extensive performance testing to evaluate the reliability of its image reconstruction algorithms and to characterize its applicability across different imaging scenarios. The key performance parameters investigated included

spatial resolution, sensitivity, and energy resolution. These evaluations required the use of both point-like and extended radioactive sources.

To assess spatial resolution, a point source, defined as having a diameter smaller than that of the scintillator pixel, was necessary. Due to the practical limitations of producing such a source with $^{99\text{m}}\text{Tc}$, a solid ^{57}Co source was employed. This isotope emits at 122 keV, serving as a suitable surrogate for the 140.5 keV photons of $^{99\text{m}}\text{Tc}$.

Conversely, the extrinsic sensitivity and energy resolution tests with $^{99\text{m}}\text{Tc}$ were performed using a custom-designed flat liquid phantom that provided uniform irradiation of the detector, as illustrated in Figure 3. Finally, additional tests were conducted with ^{177}Lu , a radionuclide used in theragnostic that emits multiple photon energies ranging from low-energy X-rays to γ emissions above 300 keV. These measurements aimed to evaluate the camera’s reconstruction performance with multi-energy emissions and to determine its suitability for imaging with ^{177}Lu .

Isotope	Energy [keV]	Window [keV]	Source form	Test
^{57}Co	122	100–140	Sealed point source	Spatial resolution, collimator leakage
$^{99\text{m}}\text{Tc}$	140.5	120–160	Flat liquid phantom	Sensitivity, Energy resolution
^{177}Lu	55–208	Multiple	Liquid source	Multi-energy reconstruction

Table 1 Summary of the radioactive sources and test conditions used to evaluate the POSiCS camera performance.

3.1 Extrinsic Spatial resolution

The extrinsic spatial resolution was assessed by placing a point-like ^{57}Co source ($E_\gamma = 122$ keV) in the center of the camera’s FOV. In this position, 100’000 events were acquired, and an image was reconstructed following the correction pipeline described in subsection 2.5. No smoothing or kernel convolution is applied to assess the device’s performance without digital image quality enhancement. An energy cut window between 100 and 140 keV was applied to reject scattered photons (cf. Figure 6). The obtained reconstructed x and y profiles were fitted with a Gaussian profile, and their full width at half maximum (FWHM) was calculated. We define the device’s resolution as the average FWHM between the two directions.

The uncertainty on the resolution is the summation in quadrature of the statistical error (obtained through the covariance matrix of the fit) and a systematic uncertainty. Systematics is defined as the variation in resolution due to the different behavior of the camera in other areas of the FOV. The systematic uncertainty is evaluated through a scan of 15 positions on the device’s FOV with the Cobalt point source, acquiring 100’000 events at each position. Each reconstructed spot is fitted with a Gaussian profile, from which the FWHM is extracted. The standard deviation of this sample

of 15 measured resolution values represents the systematic error of the resolution measurement.

The measurement at the center of the FOV is repeated for different source distances and under two conditions: with and without scattering material between the source and the camera head. The chosen scattering material is Polymethyl methacrylate (PMMA). This approach enables us to estimate the expected resolution in biological tissues, whose density is comparable to that of PMMA. The obtained resolution is also compared with the theoretical spatial resolution [27, 20, 28]:

3.2 Extrinsic sensitivity

The camera's sensitivity is defined as the registered trigger rate divided by the activity of the source within the camera's FOV. This parameter is strongly dependent on the geometry of the collimator, the efficiency of the scintillator crystal (i.e., the probability of absorbing a gamma ray through photoelectric effect at a defined energy), and the efficiency of the readout. Following the guidelines presented in the NEMA standards for gamma camera qualifications [16], we performed sensitivity measurements, ensuring that rates did not exceed 20'000 counts per second (cps).

The tests were performed by placing the flood phantom filled with Tc-99m dissolved in saline solution, to irradiate the FOV uniformly. Then, the rate was registered through the camera's wireless readout, in packets of 4000 events. The activity of the source visible in the FOV was evaluated through the following conversion:

$$A_{\text{FOV}}(t) = A(t_0) \cdot \frac{S_{\text{FOV}}}{S_{\text{FP}}} \cdot e^{-\frac{t \ln 2}{\tau_{1/2}}} \quad (3)$$

where t_0 is the source's production time (when activity was measured by a 4π detector by the Radiology department staff of the Hôpitaux Universitaires de Genève (HUG), with a precision down to tens of kBq), $\tau_{1/2} = 6.02$ h is the half-life of metastable Tc-99, S_{FOV} is the area of the FOV, and S_{FP} is the surface of the Flood Phantom. The sensitivity over time is therefore computed as:

$$g(t) = \frac{R(t)}{A_{\text{FOV}}(t)} \quad (4)$$

The reported error on the sensitivity measurements is defined as the quadrature sum of the statistical uncertainty on the rate and the systematic uncertainty on the activity, giving the uncertainty in sensitivity. The latter is the propagated error of the initial injected activity in the phantom (set at 10% of the initial activity) and the uncertainty on the custom-made phantom's dimension:

$$\sigma_{\text{sens}} = \sqrt{\frac{R(t)}{\Delta t}} \oplus \sigma_{\text{syst}} \quad (5)$$

The procedure is repeated with the LEHS collimator and the LEHR collimator, placing the source at 2cm from the camera's lid.

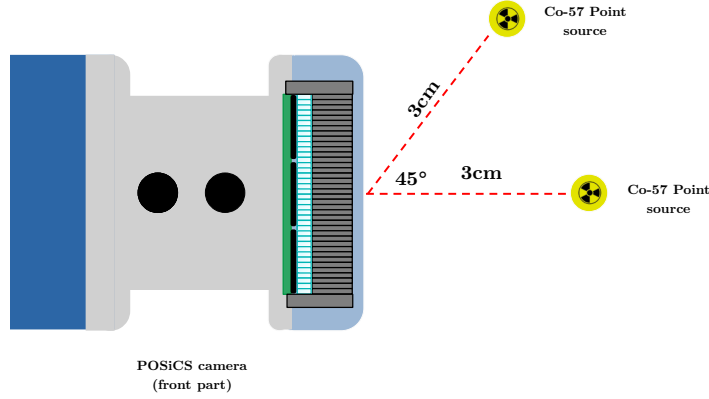


Fig. 4 Positions of the Co-57 during the evaluation of the shielding leakage. The scheme is symmetric for the third measurement (at -45°).

3.3 Energy resolution

The energy resolution was evaluated for both the LEHR and LEHS collimators by placing the Flood phantom in front of the camera to uniformly irradiate the FOV at a distance of 2 cm from the source. The resulting spectrum was corrected using a pixel-by-pixel approach, following the device's standard calibration procedure. The resolution was computed by fitting the photopeak (identified as the first and most prominent peak on the right, corresponding to the physical interaction process that leaves the most energy in the crystal) with a Gaussian profile and considering the resolution as its FWHM divided by the central theoretical energy of 140.5 keV.

3.4 Collimator septal penetration

The camera's external shielding was tested to assess the leakage of gamma rays from the Tungsten collimator's walls, which are designed to prevent external radiation from reaching the scintillator crystal. An IGC does not require strong directional sensitivity, unlike 1D gamma probes, which rely on it due to their lack of imaging capability. Directionality is, therefore, a key performance aspect typically studied in detail for probes [29]. In the case of POSiCS, a leakage study was performed to ensure that possible activity hotspots outside the FOV do not influence the imaging performance of the POSiCS camera.

This test was performed by registering the detected rate of a Co-57 point source in free air, positioned 3 cm from the center of the camera, at three distinct angles: one at 0° relative to the normal of the FOV, and the other two at 45° and -45° from the same normal direction, as shown in Figure 4. The 100-140 keV energy window (used throughout this work for Co-57 data processing) was adopted.

Rate data was collected by registering 150 packets of 4000 events for each under-test angle. For each packet, the initial and final timestamps are used to compute

the average rate of that packet. The 150 rates per angle are presented in [Figure 9](#), normalized by the mean value of the rate at 0° from the FOV normal direction.

3.5 Energy response to other radiotracers (Lu-177)

To test the camera’s performance at different γ -rays energies, we performed a study using Lu-177 as a radiotracer. This isotope has been adopted in nuclear medicine due to its multiple applications in radiotherapy [\[30, 31, 32, 33, 34\]](#). Lu-177 is often linked to peptides (such as the case of Lu¹⁷⁷-DOTA-TATE and Lu¹⁷⁷-PSMA), to target cancerous cells in several radiotherapeutic procedures, aiming to treat prostate cancer, neuroendocrine tumors, bone metastasis, and other malignancies [\[32\]](#). Lu-177 nuclei decay into Hf-177 through β^- emission. Hf-177 nuclei live in a metastable state for characteristic times of a few hundred picoseconds (depending on the state), reaching stability through the emission of gamma rays [\[30\]](#). The emission energies issued by the above-mentioned gamma dis-excitation: 208 keV (10.4% probability), 113 keV (6.2% probability), 55 keV (4.5% probability), and 65 keV (1.2% probability) [\[32, 34\]](#). Some other, less frequent energies are also present.

To perform dosimetry measurements on patients during therapy, SPECT scanners have already been used to map the activity regions traced by Lu-177 gamma-rays emission [\[31\]](#). Moreover, SFOV gamma cameras were also proposed and tested for their response to Lu177, due to the possibility of rapid scans with a smaller and more practical device [\[35\]](#). The use of handheld cameras can also contribute to pharmacokinetic studies, allowing for faster and more frequent scans [\[36\]](#).

The performance of the POSiCS camera was evaluated by imaging a 204 mm³ cavity, representing the rear tumor volume within a BIOMETECH fillable mouse phantom [\[37\]](#), depicted in [Figure 11](#). The cavity was filled with 12 MBq of Lu-177. The phantom was positioned in direct contact with the POSiCS camera, which was equipped with the LEHS collimator. Data were acquired over a total acquisition time of 100 seconds.

4 Performance results of the POSiCS camera

4.1 Extrinsic spatial resolution

The results of the spatial resolution evaluation are presented in [Figure 5](#).

By placing the source in contact with the camera, we obtained a resolution with the LEHR collimator of 1.4 ± 0.1 mm, which increased to 2.8 ± 0.1 mm when the source was moved 3 cm away. In contact with the camera head, the LEHR and LEHS collimators show comparable resolutions. However, due to the well-known collimator projective effect [\[20, 27\]](#), the slope of the resolution over distance for the LEHS collimator shows a much steeper trend. With the latter collimator, we measured a spatial resolution of 1.9 ± 0.1 mm at 0 cm from the source, which increased to 5.1 ± 0.1 mm at 3 cm. Moreover, the difference between measurements in free air and with scatterer material is within error bars using the LEHR collimator, while the presence of PMMA worsens resolution with the LEHS collimator. This phenomenon is likely related to the

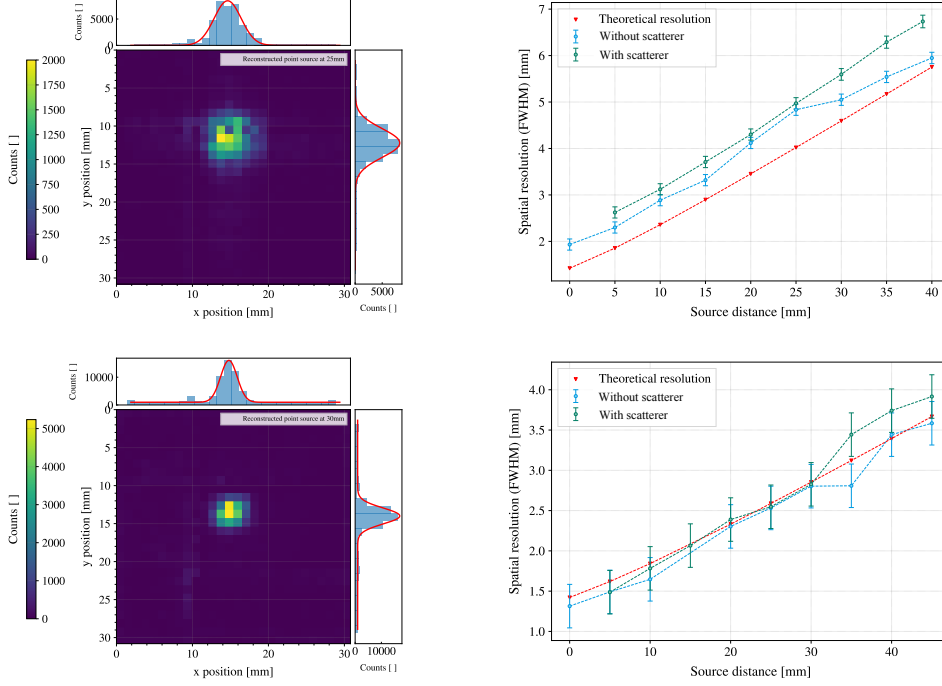


Fig. 5 **Top Left:** Example of the reconstructed point source at 3 cm from the camera (free air) with LEHS collimator. **Top Right:** Resolution of the POSiCS camera in HS mode for different distances. **Bottom Left:** Example of the reconstructed point source at 3 cm from the camera (free air) with LEHR collimator. **Bottom Right:** Resolution of the POSiCS camera in HR mode.

collimator's improved ability to reject photons scattered in the PMMA layers between the source and the camera.

For the LEHS collimator, the measured extrinsic resolution in free air is larger than the theoretical one by 15% on average, as displayed in Figure 5 (top Right). This inconsistency, which lies beyond error bars, is mainly due to the light detector and the thin collimator septa. Theoretical calculations, indeed, do not consider the resolution spread due to the light detector, which, in our case, presents some deformations toward the interstitial gaps between SiPMs, for instance. Moreover, for a short collimator with thin septa, it is possible to have an increased septal penetration, and therefore a reduced spatial resolution, which is challenging to estimate empirically. Consequently, we can conclude that the camera's extrinsic resolution aligns reasonably well with theoretical expectations, showing a similar slope as the distance increases. The LEHR collimator analysis reveals a more precise agreement with theoretical expectations, likely due to the reduced number of accepted scattered photons and reduced septal penetration.

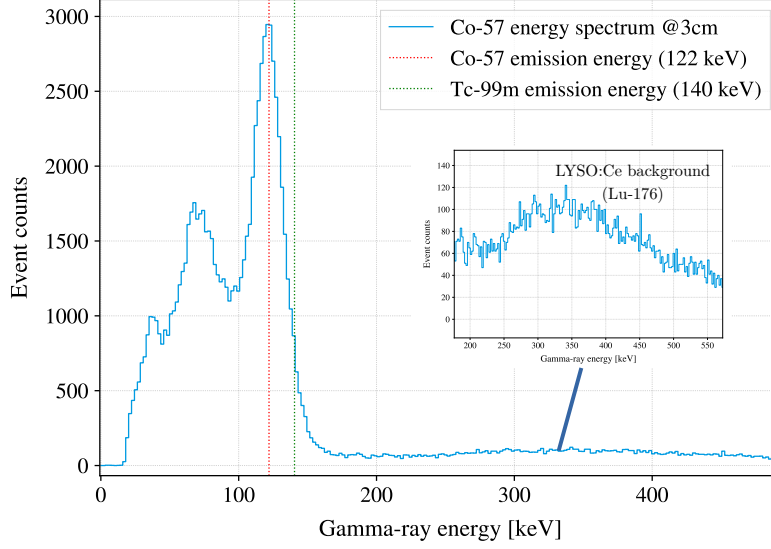


Fig. 6 Example of energy spectrum of the Co-57 point source positioned 3 cm from the center of the camera FOV (LEHR collimator). The background-dominated region associated with LYSO intrinsic radioactivity is highlighted, illustrating that it does not significantly contribute to the energy window centered around 122 keV

Sensitivity results	LEHS collimator	LEHR collimator
Sensitivity BEC [cps/MBq]	1444 ± 31	730 ± 16
Sensitivity AEC [cps/MBq]	481 ± 14	134 ± 8
Theoretical sensitivity [cps/MBq]	591	140
Distribution Kurtosis	2.89	2.97
Distribution skewness	0.04	0.00

Table 2 Sensitivity results compared to the theoretical expectations. BEC = Before Energy Cut, AEC = After Energy Cut.

4.2 Extrinsic sensitivity

For the LEHS mode camera, we report a sensitivity of 481 ± 14 cps/MBq after rejecting all events whose energy does not lie within the spectral window adopted in this work for Tc-99m (120 keV-160 keV). Instead, we observe a significant reduction in sensitivity for the LEHR collimator, down to 134 ± 8 cps/MBq. We identify the reason for the mismatch between theoretical predictions and the actual detected sensitivity (about 4%-20%, depending on the collimator) as being related to the choice of energy window containing photoelectric absorption events and the uncertainty the image correction algorithm adds.

The results of the sensitivity evaluation are displayed in Figure 7 for both collimators. For the camera in HR mode, we observed a measured sensitivity distributed as a

Gaussian function around its central value, with a standard deviation of 6 cps/MBq. This is displayed in the sensitivity projection on the right side-plot. The Gaussianity of this distribution implies that the negative exponential decay correction to the activity matches the observed rate. Furthermore, from [Table 2](#), we evince that the Skewness and Kurtosis of the points distribution (side plot) are compatible with a Gaussian distribution, for which the typical skewness is 0 and the typical kurtosis is 3. For the LEHS collimator, we observe a distribution of sensitivities characterized by a slight positive skewness (indicating a heavier right tail) and a kurtosis slightly below 3, which suggests a more peaked distribution. This is also evident in the time series of measured sensitivities, which shows a positive vertical bending of the estimated sensitivity around 600 s (cf. [Figure 7](#)). We identify this problem with the high count rate registered with the high-sensitivity collimator, suggesting that saturation effects are beginning to build up. Therefore, the results we obtained should be considered a lower limit on the sensitivity, which could be higher if a lower-activity source had been placed in front of the camera.

4.3 Energy resolution

The achieved energy resolution with the LEHS collimator is 19.14%, which aligns with the typical energy resolutions reported in the literature for SFOV gamma cameras [\[4\]](#). However, this result is relatively sharp for a LYSO-based device [\[38, 39, 40\]](#). This energy resolution is enough to distinguish the photopeak from the nearby structures in the energy spectrum, namely the backscattering peak (located at about 90 keV, as expected) and the Compton edge: the third peak from the Right in [Figure 8](#).

With the LEHR collimator, it was possible to measure an energy resolution of 19.94%, which, as expected, is comparable with the resolution achieved through the LEHS collimator. Energy resolution is primarily driven by the scintillator (the number of photons produced per scintillation event), the optical coupling to the photodetector, and the photodetector efficiency. Therefore, as assessed by these tests, the collimator does not significantly impact the energy resolution. However, we notice a large amount of scattered gamma rays with the LEHR collimator, which we link to the increased amount of high-Z scatterer material (tungsten) present due to the longer collimator.

4.4 Collimator septal penetration

The tests with both collimators show that the count rate drops significantly when the source is placed outside of the FOV. Moreover, the response is symmetric when placing the source outside of the FOV to the left and Right of the camera. In the case of the LEHS collimator, the average rate drop outside the FOV is 88%, indicating that the shielding around the scintillator effectively eliminates most of the incoming gamma rays. The LEHR collimator shows an average relative rate drop of only 61%. Since both collimators have the same shielding thickness, the observed discrepancy may suggest that the greater amount of tungsten in the LEHR collimator leads to increased gamma-ray scattering. As a result, Compton-scattered gamma rays may still reach the scintillator and be detected. This implies that the energy window cut applied around the photopeak is less effective when using the LEHR collimator.

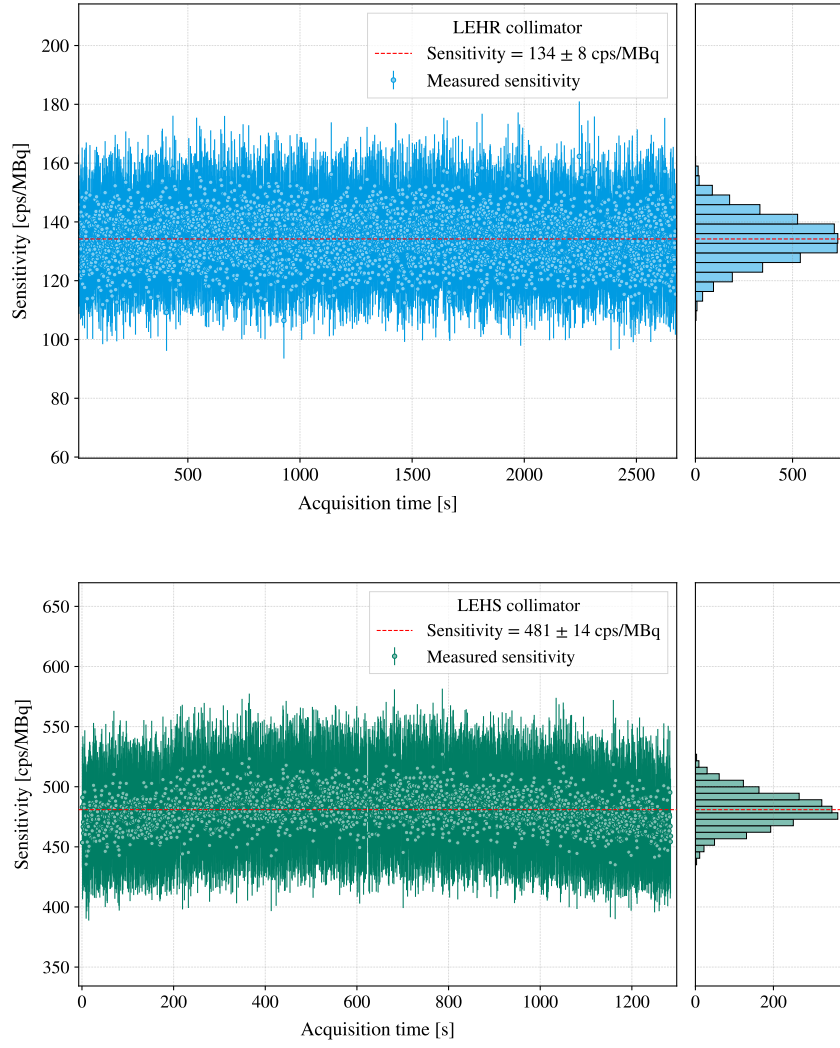


Fig. 7 Top: Sensitivity over time of the camera in HR mode at 2cm from the source, after energy window cut (120-160 keV). **Bottom:** Sensitivity over time of the camera in HS mode at 2cm from the source, after energy window cut.

4.5 Camera's response to other radiotracers (Lu-177)

With the device under test, it was possible to observe a Lu-177 source emitting at different energies.

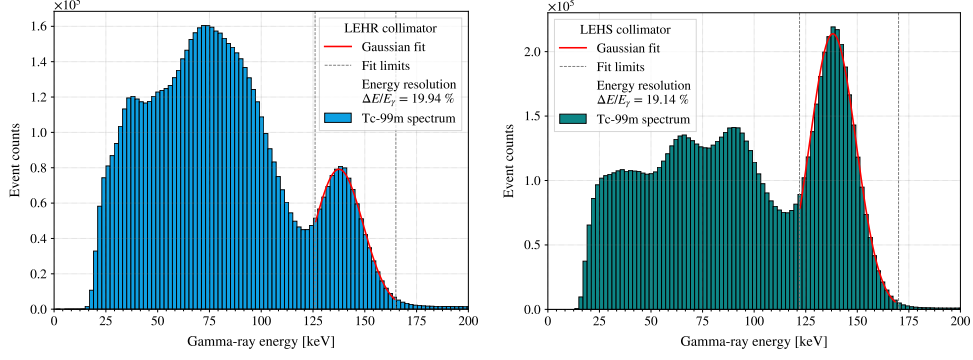


Fig. 8 Left: Corrected spectrum obtained with POSiCS (LEHR collimator) over the whole UFOV. **Right:** Corrected spectrum obtained with POSiCS (LEHR collimator) over the whole UFOV. Compton backscattering and Compton edge peaks are visible, before the photopeak at 140 keV.

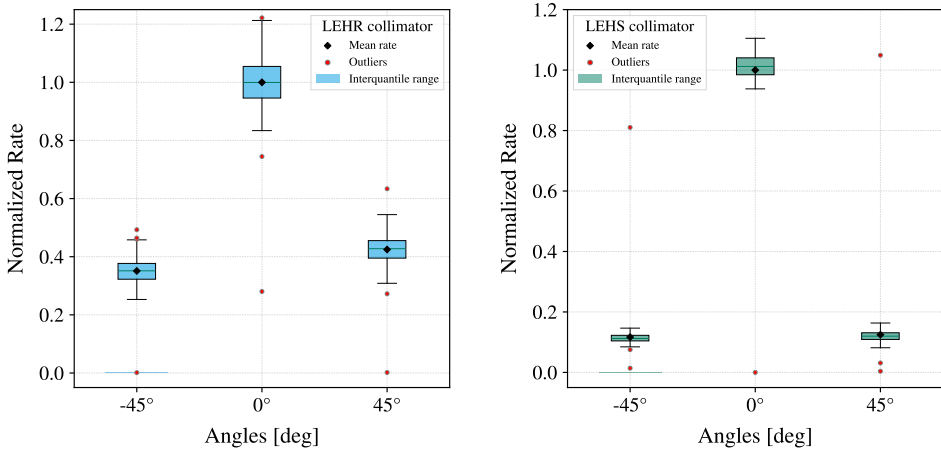


Fig. 9 Left: Leakage test results for the LEHR collimator. **Right:** Leakage test results for the LEHS collimator.

The obtained energy spectrum is displayed in [Figure 10](#). The main emission peak was found to be at 218 keV, which shows, therefore, a 4.6% discrepancy with the theoretical value (208 keV). This behaviour is expected, since the camera was calibrated based on a 140 keV reference energy, and the non-linearity of the camera's light detector charge response creates a slight shift in the central energy value. For this reason, the energy look-up table (LUT) was rescaled to ensure that the main emission peak was centered at 208 keV. With this correction, it was possible to identify the peaks presented in [Table 3](#).

We recognize the first peak as very low-energy X-rays and background radiation. We identify peak number 2 as the X-ray emissions at 55 keV and 64 keV, which merge into a single peak at 60 keV due to the limited energy resolution of the camera at such low energies, as already observed by [\[34\]](#). Peak number 3 is the 113 keV

emission, which is clearly distinguishable and well centered around its reference value. We identify peak number 4 as the Compton shoulder of the main emission line (peak 5). It is also possible to notice a small bump in the spectrum after the 208 keV energy, which could correspond to a weak emission of Lu-177 (321 keV). However, this energy has a low photoelectric absorption probability within the thin scintillator crystal of the POSiCS camera and, therefore, cannot be identified. Moreover, this higher-energy region is also populated by the Lu-176 background due to the presence of this isotope in the LYSO:Ce scintillator (cf. subsection 2.3).

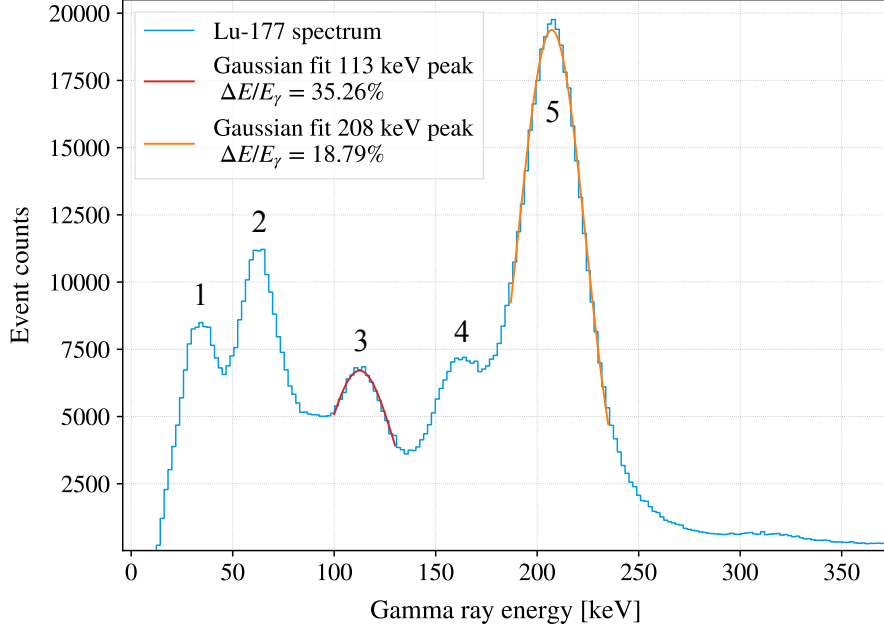


Fig. 10 Recorded and rescaled spectrum obtained through the mice-phantom cavity measurement.

The primary emission energies used for Lu-177 SPECT imaging are the 113 keV and 208 keV gamma-rays. In our case, the energy resolution of these two photopeaks was determined through a Gaussian fit and found to be 35% and 19%, respectively. We therefore proceeded with the usual calibration pipeline, by defining two 20% energy windows around these peaks (following the approach of [32]) and a large energy window (0-76 keV) to assess the reconstructed images through low-energy X-ray emission.

The imaging results after the standard image correction pipeline, Gaussian kernel convolution (following the NEMA standards guidelines [16]), and spline interpolation, are presented in Figure 11. The cavity image can be efficiently reconstructed for both the X-ray and 113 keV energy windows. However, we encounter significant problems in reliably reconstructing an image at 208 keV. As the Figure 11 shows, gamma-ray

Peak number	Central energy	Energy resolution
Peak 1	34 keV	-
Peak 2	60 keV	-
Peak 3	113 keV	35%
Peak 4	163 keV	-
Peak 5	208 keV	19%

Table 3 Identified peaks in the measured, calibrated, and rescaled Lu-177 energy spectrum. The energy resolution is also presented for the two peaks of interest for imaging.

POSiCS camera performance	LEHS collimator	LEHR collimator
Spatial resolution		
Spatial resolution AEC (122 keV) @0cm [mm]	1.9 ± 0.1	1.4 ± 0.3
Spatial resolution AEC (122 keV) @3cm [mm]	5.1 ± 0.1	2.8 ± 0.3
Sensitivity		
Sensitivity BEC (140.5 keV) @2cm [cps/MBq]	1444 ± 31	730 ± 16
Sensitivity AEC (140.5 keV) @2cm [cps/MBq] *	481 ± 14	134 ± 8
Other parameters		
Energy resolution (140.5 keV) @2cm	19%	20%
Rate drop outside FOV (122 keV) @3cm	88%	61%
Field Of View (FOV)	$30.8 \times 30.8 \text{ mm}^2$	$30.8 \times 30.8 \text{ mm}^2$
Useful Field Of View (UFOV)	$28.6 \times 28.6 \text{ mm}^2$	$28.6 \times 28.6 \text{ mm}^2$

Table 4 Performance parameters results presented in this work. * Lower limit of the sensitivity for this collimator. BEC = Before Energy Cut, AEC = After Energy Cut

detection in the 208 keV range extends beyond the cavity’s region of interest (ROI), with signals detected in pixels outside the area filled with activity. This issue arises from the use of thin collimator septa, which are optimized for lower energies and fail to constrain non-perpendicular gamma rays at 208 keV adequately.

This test demonstrated that the POSiCS camera, without any modification to its configuration or components, is also suitable for imaging with Lu-177. It effectively detects events associated with the isotope’s X-ray emissions as well as gamma emissions up to its 133 keV peak. However, imaging at higher energies would require the use of a longer collimator. The performance of the current LEHR collimator with Lu-177 is presently under investigation.

4.6 Performance parameters discussion

Table 4 provides a summary of the key performance parameters of the POSiCS camera. The results confirm that the system fulfills its intended purpose, enabling imaging with millimeter-scale spatial resolution: a critical feature for intraoperative applications. Notably, when equipped with the LEHS collimator, the camera achieves

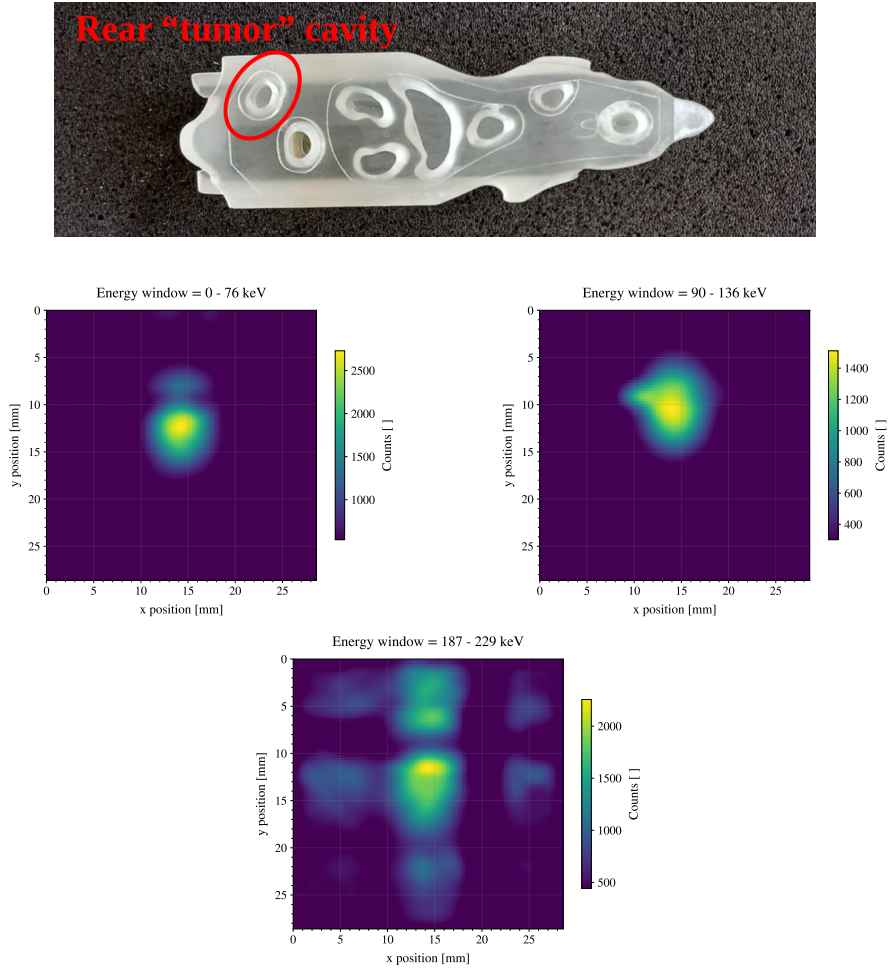


Fig. 11 Top: Bioemtech Mice Phantom used for the Lu-177 test. The rear "tumor" cavity was filled with the radiotracer and covered by the phantom's plastic lid. Phantom from [37]. **Bottom:** Reconstructed cavity image for three different energy windows after triple correction (Linearity, Energy cut, and uniformity compensation), treated with Gaussian kernel and spline interpolation.

high sensitivity compared to other intraoperative gamma systems used for radioguided surgery (RGS) [4]. This is particularly advantageous for rapid image acquisition, minimizing disruptions to the surgical workflow.

The measured energy resolution is generally broader compared to other scintillator cameras with higher light yields, such as $\text{LaBr}_3\text{:Ce}$ or the more commonly used NaI:Tl cameras (or if compared to direct-detection gamma cameras, such as CZT-based devices). Nevertheless, the observed resolution remains competitive, especially when compared to larger LYSO-based systems operating near 140 keV, which often

exhibit energy resolutions exceeding 20%. Moreover, LYSO offers additional benefits: its high density allows for the development of compact detectors with enhanced sensitivity.

Shielding tests revealed some residual gamma-ray penetration from the sides and indicated significant scattering associated with the LEHR collimator. This is also evidenced by the corresponding energy spectrum acquired with the same scintillator (see [Figure 8](#)). An improved collimator design with enhanced lateral shielding could further mitigate this scattering and leakage.

5 Outlook and future developments

The POSiCS camera was developed as a lightweight, compact, and wireless IGC to assist surgeons during SLNB and ROLL procedures. Integrating rapid, user-friendly imaging systems in surgical settings can reduce procedural invasiveness, thus enhancing both treatment efficacy and postoperative outcomes.

POSiCS demonstrated high spatial resolution when equipped with a LEHR collimator and showed good sensitivity in its LEHS collimator configuration. By comparing the results described in this work with current state-of-the-art IGCs, we demonstrate that POSiCS performances are comparable to, or superior to, currently available systems [4, 7], while offering additional benefits, such as a lightweight module (less than 400 g) and wireless communication. These features significantly improve usability within the surgical environment. The most critical performance parameters determined through the tests described in this work are summarized in [Table 4](#).

Furthermore, the camera successfully detected gamma emissions from lutetium-177, demonstrating imaging capability up to the 113 keV photon emission line of this isotope. It was also possible to produce reliable images of the source by detecting lower-energy X-rays. These findings suggest that the device’s field of applications extends beyond traditional techniques involving the administration of Tc-99m, and may be suited for applications in theranostics and radiotherapeutic dosimetry, without the need for modifications to the detector system.

Acknowledgments

This study was conducted as part of the POSiCS project. The POSiCS project is being carried out jointly by a consortium between [University of Geneva \(UNIGE\)](#), [PIN lab](#) at Hôpitaux Universitaires de Genève (HUG), and [Fondazione Bruno Kessler \(FBK\)](#) in Italy. POSiCS was funded for the second phase of the ATTRACT European initiative in June 2022, following the Horizon 2020 call. The Consortium Partners receive funding from the European Union for ATTRACT under Grant Agreement no. 101004462 and the Horizon 2020 Framework Programme for Research and Innovation (2014–2020). The position-sensitive LG-SiPM is based on the patented technology (EP3063559) developed by FBK.

References

- [1] Giuliano Mariani, Luciano Moresco, Giuseppe Viale, Giuseppe Villa, Marcello Bagnasco, Giuseppe Canavese, John Buscombe, H. William Strauss, and Giovanni Paganelli. Radioguided sentinel lymph node biopsy in breast cancer surgery*. *Journal of Nuclear Medicine*, 42(8):1198–1215, 2001. ISSN 0161-5505. URL <https://jnm.snmjournals.org/content/42/8/1198>.
- [2] Giuliano Mariani, Marco Gipponi, Luciano Moresco, Giuseppe Villa, Mirco Bartolomei, Giovanni Mazzarol, Maria Claudia Bagnara, Antonella Romanini, Ferdinando Cafiero, Giovanni Paganelli, and H. William Strauss. Radioguided sentinel lymph node biopsy in malignant cutaneous melanoma*. *Journal of Nuclear Medicine*, 43(6):811–827, 2002. ISSN 0161-5505. URL <https://jnm.snmjournals.org/content/43/6/811>.
- [3] Hossein Arabi, Abdollah Saberi Manesh, and Habib Zaidi. Innovations in dedicated pet instrumentation: from the operating room to specimen imaging. *Physics in Medicine & Biology*, 69(11):11TR03, may 2024. doi: 10.1088/1361-6560/ad4b92. URL <https://dx.doi.org/10.1088/1361-6560/ad4b92>.
- [4] Andrew L. Farnworth and Sarah L. Bugby. Intraoperative gamma cameras: A review of development in the last decade and future outlook. *Journal of Imaging*, 9, 05 2023. ISSN 2313433X. doi: 10.3390/jimaging9050102.
- [5] I Stoffels, T Poeppel, C Boy, S Mueller, F Wichmann, J Dissemmond, D Schaden-dorf, S Rosenbaum-Krumme, and J Klode. Radio-guided surgery: advantages of a new portable γ -camera (sentinella) for intraoperative real time imaging and detection of sentinel lymph nodes in cutaneous malignancies. *Journal of the European Academy of Dermatology and Venereology*, 26(3):308–313, 2012. ISSN 1468-3083. doi: 10.1111/j.1468-3083.2011.04057.x. Epub 2011 Mar 23.
- [6] Roberto Massari, Antonio Ucci, Annunziata D’Elia, Costantino Campisi, Emilio Bertani, and Alessandro Soluri. Directional probe for radio-guided surgery: A pilot study. *Medical Physics*, 45(2):622–628, 2018. ISSN 2473-4209. doi: 10.1002/mp.12726. Epub 2018 Jan 2.
- [7] Makoto Tsuchimochi and Kazuhide Hayama. Intraoperative gamma cameras for radioguided surgery: Technical characteristics, performance parameters, and clinical applications. *Physica Medica*, 29(2):126–138, 2013. ISSN 1120-1797. doi: <https://doi.org/10.1016/j.ejmp.2012.05.002>. URL <https://www.sciencedirect.com/science/article/pii/S1120179712000397>.
- [8] Daan Hellingman and Sergi Vidal-Sicart. *The Use of Intraoperative Small and Large Field of View Gamma Cameras for Radioguided Surgery*, pages 35–56. Springer International Publishing, Cham, 2016. ISBN 978-3-319-26051-8. doi: 10.1007/978-3-319-26051-8_3. URL https://doi.org/10.1007/978-3-319-26051-8_3.
- [9] P. Paredes, S. Vidal-Sicart, G. Zanón, N. Roé, S. Rubí, S. Lafuente, J. Pavía, and F. Pons. Radioguided occult lesion localisation in breast cancer using an intraoperative portable gamma camera: first results. *European Journal of Nuclear Medicine and Molecular Imaging*, 35(2):230–235, Feb 2008. ISSN 1619-7089. doi: 10.1007/s00259-007-0640-x. URL <https://doi.org/10.1007/s00259-007-0640-x>.

- [10] A. Soluri, R. Massari, C. Trotta, A. Tofani, G. Di Santo, B. Di Pietro, M.L. Di Paolo, A. Roncacci, C. Amanti, and F. Scopinaro. Small field of view, high-resolution, portable *gamma*-camera for axillary sentinel node detection. *Nuclear Instruments and Methods in Physics Research Section A: Accelerators, Spectrometers, Detectors and Associated Equipment*, 569(2):273–276, 2006. ISSN 0168-9002. doi: <https://doi.org/10.1016/j.nima.2006.08.027>. URL <https://www.sciencedirect.com/science/article/pii/S0168900206014513>. Proceedings of the 3rd International Conference on Imaging Technologies in Biomedical Sciences.
- [11] G. H. KleinJan, A. Bunschoten, O. R. Brouwer, N. S. van den Berg, R. A. Valdés-Olmos, and F. W. B. van Leeuwen. Multimodal imaging in radioguided surgery. *Clinical and Translational Imaging*, 1(6):433–444, Dec 2013. ISSN 2281-7565. doi: [10.1007/s40336-013-0039-6](https://doi.org/10.1007/s40336-013-0039-6). URL <https://doi.org/10.1007/s40336-013-0039-6>.
- [12] Fabio Acerbi, Stefano Merzi, and Alberto Gola. Position-sensitive silicon photomultiplier arrays with large-area and sub-millimeter resolution. *Sensors*, 24, 7 2024. ISSN 14248220. doi: [10.3390/s24144507](https://doi.org/10.3390/s24144507).
- [13] Aramis Raiola, Fabio Acerbi, Cyril Alispach, Hossein Arabi, Domenico della Volpe, Alberto Gola, and Habib Zaidi. Quantitative determination of spatial resolution and linearity of position-sensitive lg-sipms at sub-millimeter scale via ricean distribution fitting. *Nuclear Instruments and Methods in Physics Research Section A: Accelerators, Spectrometers, Detectors and Associated Equipment*, 1080:170774, 2025. ISSN 0168-9002. doi: <https://doi.org/10.1016/j.nima.2025.170774>. URL <https://www.sciencedirect.com/science/article/pii/S0168900225005753>.
- [14] Alberto Gola, Alessandro Ferri, Alessandro Tarolli, Nicola Zorzi, and Claudio Piemonte. A novel approach to position-sensitive silicon photomultipliers: First results. *2013 IEEE Nuclear Science Symposium and Medical Imaging Conference (2013 NSS/MIC)*, pages 1–4, 2013. URL <https://api.semanticscholar.org/CorpusID:24489596>.
- [15] Fabio Acerbi, Stefano Merzi, and Alberto Gola. Large area tiles of position-sensitive silicon photomultipliers. In *Proceedings of the 13th International Conference on Position Sensitive Detectors (PSD13)*, Oxford, United Kingdom, September 2023. Fondazione Bruno Kessler (FBK). URL [https://indico.global/event/1725/contributions/30421/attachments/15498/24679/Acerbi%20-%20PS-SiPM_\(PSD13\)_r4b.pdf](https://indico.global/event/1725/contributions/30421/attachments/15498/24679/Acerbi%20-%20PS-SiPM_(PSD13)_r4b.pdf). Presentation slides.
- [16] National Electrical Manufacturers Association. *Performance Measurements of Gamma Cameras*. NEMA, Rosslyn, VA, 2023. NEMA NU 1-2023.
- [17] Fabio Acerbi, Aramis Raiola, Cyril Alispach, Hossein Arabi, Habib Zaidi, Alberto Gola, and Domenico Della Volpe. Compact and handheld sipm-based gamma camera for radio-guided surgery and medical imaging. *Instruments*, 9(2), 2025. ISSN 2410-390X. doi: [10.3390/instruments9020014](https://doi.org/10.3390/instruments9020014). URL <https://www.mdpi.com/2410-390X/9/2/14>.
- [18] S Jan, G Santin, D Strul, S Staelens, K Assié, D Autret, S Avner, R Barbier, M Bardiès, P M Bloomfield, et al. Gate: a simulation toolkit for pet and spect. *Physics in Medicine & Biology*, 49(19):4543, 2004.

- [19] Stephen C. Moore, Kypros Kouris, and Ian Cullum. Collimator design for single photon emission tomography. *European Journal of Nuclear Medicine*, 19(2):138–150, 02 1992. ISSN 1619-7089. doi: 10.1007/BF00184130. URL <https://doi.org/10.1007/BF00184130>.
- [20] Simon R. Cherry, James A. Sorenson, and Michael E. Phelps. chapter 14 - the gamma camera: Performance characteristics. In Simon R. Cherry, James A. Sorenson, and Michael E. Phelps, editors, *Physics in Nuclear Medicine (Fourth Edition)*, pages 209–231. W.B. Saunders, Philadelphia, fourth edition edition, 2012. ISBN 978-1-4160-5198-5. doi: <https://doi.org/10.1016/B978-1-4160-5198-5.00014-9>. URL <https://www.sciencedirect.com/science/article/pii/B9781416051985000149>.
- [21] T. Kimble, M. Chou, and B.H.T. Chai. Scintillation properties of lyso crystals. In *2002 IEEE Nuclear Science Symposium Conference Record*, volume 3, pages 1434–1437 vol.3, 2002. doi: 10.1109/NSSMIC.2002.1239590.
- [22] Maurizio Conti, Lars Eriksson, Harold Rothfuss, Therese Sjoeholm, David Townsend, Göran Rosenqvist, and Thomas Carlier. Characterization of 176lu background in lso-based pet scanners. *Physics in Medicine & Biology*, 62(9):3700, apr 2017. doi: 10.1088/1361-6560/aa68ca. URL <https://dx.doi.org/10.1088/1361-6560/aa68ca>.
- [23] Héctor Alva-Sánchez, Alejandro Zepeda Barrios, Victor Daniel Díaz Martínez, Tirso Murrieta, A. Martínez-Dávalos, and Mercedes Rodríguez-Villafuerte. Understanding the intrinsic radioactivity energy spectrum from 176lu in lyso/lso scintillation crystals. *Scientific Reports*, 8, 11 2018. doi: 10.1038/s41598-018-35684-x.
- [24] Qingyang Wei, Shi Wang, Tiantian Dai, Tianyu Ma, Hui Liu, Jing Wu, Nianming Jiang, Zhaoxia Wu, and Yaqiang Liu. Geometrical calibration of a pet-scanner-based multi-pinhole spect using lyso background radiation. In *2014 IEEE Nuclear Science Symposium and Medical Imaging Conference (NSS/MIC)*, pages 1–4, 2014. doi: 10.1109/NSSMIC.2014.7431011.
- [25] Alessandro Ferri, Fabio Acerbi, Alberto Gola, G. Paternoster, Claudio Piemonte, and Nicola Zorzi. Characterization of linearly graded position-sensitive silicon photomultipliers. *EJNMMI Physics*, 1:A14, 07 2014. doi: 10.1186/2197-7364-1-S1-A14.
- [26] Fabio Acerbi, Diego Tanagni, Tommaso Marchi, Benito Gongora Servin, A. Celenzano, R. Bolzonella, A. Goasduff, J. J. Valiente Dobon, F. Gramegna, Gianmaria Collazuol, and Alberto Gola. Reduced-channels position-sensitive 10x1 sipm tile for scintillator-bars readout. *IEEE Transactions on Nuclear Science*, 2024. ISSN 15581578. doi: 10.1109/TNS.2024.3489713.
- [27] Hal O. Anger. Scintillation camera. *Review of Scientific Instruments*, 29(1):27–33, 01 1958. ISSN 0034-6748. doi: 10.1063/1.1715998. URL <https://doi.org/10.1063/1.1715998>.
- [28] M. J. Berger, J. H. Hubbell, S. M. Seltzer, J. Chang, J. S. Coursey, R. Sukumar, D. S. Zucker, and K. Olsen. XCOM: Photon Cross Section Database (version 1.5). <http://physics.nist.gov/xcom>, 2010. National Institute of Standards and Technology, Gaithersburg, MD. Accessed: 2025-04-13.

- [29] Dariusz Wydra, Rafał Matuszewski, Grzegorz Romanowicz, and Tomasz Bandurski. Evaluation of surgical gamma probes for sentinel node localization in cervical and vulvar cancer. *Nuclear Medicine Review. Central & Eastern Europe*, 8(2):105–110, 2005. ISSN 1506-9680. Evaluation Study; PMID: 16437395.
- [30] Mauro S. Dias, Fabrício F.V. Silva, and Marina F. Koskinas. Standardization and measurement of gamma-ray probability per decay of ^{177}Lu . *Applied Radiation and Isotopes*, 68:1349–1353, 7 2010. ISSN 09698043. doi: 10.1016/j.apradiso.2009.12.023.
- [31] Michael Ljungberg, Anna Celler, Mark W. Konijnenberg, Keith F. Eckerman, Yuni K. Dewaraja, and Katarina Sjögren-Gleisner. MIRD pamphlet no. 26: Joint EANM/MIRD guidelines for quantitative ^{177}Lu SPECT applied for dosimetry of radiopharmaceutical therapy. *Journal of Nuclear Medicine*, 57:151–162, 1 2016. ISSN 01615505. doi: 10.2967/jnumed.115.159012.
- [32] Gwennaëlle Marin, Bruno Vanderlinden, Ioannis Karfis, Thomas Guiot, Zena Wimana, Patrick Flamen, and Stefaan Vandenberghe. Accuracy and precision assessment for activity quantification in individualized dosimetry of ^{177}Lu -DOTATATE therapy. *EJNMMI Physics*, 4, 12 2017. ISSN 21977364. doi: 10.1186/s40658-017-0174-7.
- [33] Keamogetswe Ramonaheng, Milani Qebetu, Honest Ndlovu, Cecile Swanepoel, Liani Smith, Sipho Mdanda, Amanda Mdlophane, and Mike Sathekge. Activity quantification and dosimetry in radiopharmaceutical therapy with reference to ^{177}Lu -tutetium, 2024. ISSN 26738880.
- [34] Yuri Sagisaka, Yasuyuki Takahashi, Shota Hosokawa, Niina Kanazawa, Hiroki Yamamoto, Go Takai, and Keiji Nagano. Acquisition conditions for ^{177}Lu -DOTATATE imaging. *Radiation*, 4:17–25, 1 2024. doi: 10.3390/radiation4010002.
- [35] Daniel Roth, Erik Larsson, Anna Sundlöf, and Katarina Sjögren-Gleisner. Characterisation of a hand-held CZT-based gamma camera for ^{177}Lu imaging. *EJNMMI Physics*, 7(1):46, 2020. ISSN 2197-7364. doi: 10.1186/s40658-020-00313-y. URL <https://doi.org/10.1186/s40658-020-00313-y>.
- [36] Daniel Roth, Erik Larsson, Joanna Strand, Michael Ljungberg, and Katarina Sjögren-Gleisner. Feasibility of (^{177}Lu) activity quantification using a small portable CZT-based gamma-camera. *EJNMMI Physics*, 11(1):2, 2024. doi: 10.1186/s40658-023-00602-2. URL <https://doi.org/10.1186/s40658-023-00602-2>. Published online 2024 Jan 3.
- [37] Biometech AB. Fillable mouse phantom for preclinical imaging. <https://www.biometech.se>, 2024. Accessed: 2025-04-25.
- [38] Kouhei Nakanishi, Seiichi Yamamoto, and Jun Kataoka. Performance comparison of finely pixelated LySO- and GAGG-based SiPM gamma cameras for high resolution SPECT. *Nuclear Instruments and Methods in Physics Research, Section A: Accelerators, Spectrometers, Detectors and Associated Equipment*, 872:107–111, November 2017. ISSN 0168-9002. doi: 10.1016/j.nima.2017.08.013. Publisher Copyright: © 2017 Elsevier B.V.
- [39] Karel Deprez, Roel Van Holen, and Stefaan Vandenberghe. A high resolution SPECT detector based on thin continuous LySO. *Physics in Medicine & Biology*, 59(1):153, dec 2013. doi: 10.1088/0031-9155/59/1/153. URL <https://dx.doi.org/>

[10.1088/0031-9155/59/1/153](https://doi.org/10.1088/0031-9155/59/1/153).

- [40] A Morozov, F Alves, J Marcos, R Martins, L Pereira, V Solovov, and V Chepel. Iterative reconstruction of sipm light response functions in a square-shaped compact gamma camera. *Physics in Medicine & Biology*, 62(9):3619, apr 2017. doi: 10.1088/1361-6560/aa6029. URL <https://dx.doi.org/10.1088/1361-6560/aa6029>.